1   19 October 2016

3   Improved retrieval of land ice topography from CryoSat-2 data and its

4   impact for volume change estimation of the Greenland Ice Sheet

5   Johan Nilsson[1], Alex Gardner[1], Louise Sandberg Sørensen[2] and Rene Forsberg[2]

6   [1]Jet Propulsion Laboratory, California University of Technology

7   [2]DTU Space, National Space Institute, Technical University of Denmark

8   Abstract

9   A new methodology for retrieval of glacier and ice sheet elevations and elevation changes from

10   CryoSat-2 data is presented. Surface elevations and elevation changes determined using this

11   approach show significant improvements over ESA's publically available Cryosat-2 elevation

12   product (L2 Baseline-B). The results are compared to near-coincident airborne laser altimetry

13   from NASA's Operation IceBridge and seasonal height amplitudes from the Ice, Cloud, and

14   Elevation Satellite (ICESat).

15   Applying this methodology to CryoSat-2 data collected in Interferometric Synthetic

16   Aperture mode (SIN) over the high relief regions of the Greenland ice sheet we find an

17   improvement in the root-mean-square-error (RMSE) of 27% and 40% compared to ESA's L2

18   product in the derived elevation and elevation changes, respectively. In the interior part of the

19   ice sheet, where CryoSat-2 operates in Low Resolution Mode (LRM), we find an improvement in

20   the RMSE of 68% and 55% in the derived elevation and elevation changes, respectively. There

21   is also an 86% improvement in the magnitude of the seasonal amplitudes when compared to

22   amplitudes derived from ICESat data. These results indicate that the new methodology provides

23 improved tracking of the snow/ice surface with lower sensitivity to changes in near-surface

24 dielectric properties.

25   To demonstrate the utility of the new processing methodology we produce elevations,

26 elevation changes and total volume changes from Cryosat-2 data for the Greenland Ice Sheet

27 during the period Jan-2011 to Jan-2015. We find that the Greenland Ice Sheet decreased in

28 volume at rate of 289 ± 20 $km^3 a^{-1}$, with high inter-annual variability and spatial heterogeneity in

29 rates of loss. This rate is 65 $km^3 a^{-1}$ more negative than rates determined from ESA's L2

30 product, highlighting the importance of Cryosat-2 processing methodologies.

31 1 - Introduction

32 The European Space Agency (ESA) launched CryoSat-2 in April 2010 tasked with monitoring

33 the changes of the Earth's land and sea ice. CryoSat-2 carries a new type of Doppler/delay

34 radar altimeter (Raney, 1998) referred to as SIRAL (SAR Interferometric Radar Altimeter).

35 SIRAL operates in two different modes over land ice. Over the interior part of the ice sheets it

36 operates as a conventional pulse limited radar system, referred to as the "Low Resolution

37 Mode" (LRM). In more complex high-sloping terrain the system uses a novel second antenna to

38 operate in "Interferometric Synthetic Aperture Radar" (SIN) mode. This new feature allows the

39 satellite to monitor changes in complex terrain including ice caps, glaciers and the high relief

40 marginal areas of the ice sheets. Such areas are sensitive to changes in climate and contribute

41 greatly to current rates of sea level rise (e.g., Gardner et al. (2013) and Shepherd et al. (2012)).

42   Ku-band radar altimeters are insensitive to cloud cover providing superior coverage to

43 laser altimeters (e.g., ICESat) but experience significant amounts of volume scattering, which is

44 controlled by the time-evolving dielectric properties of the near-surface snow, firn, and ice

45 (Lacroix et al., 2008; Remy et al., 2012). These effects can have large implications for the

46 determination of mass change over a wide range of both spatial and temporal scales. Changing

47 snow conditions can introduce time-varying biases in the data that, in combination with the radar

48   signals interaction with the surface, introduce large elevation biases (0.5 - 1 m) (Nilsson et al.,

49   2015a). This, combined with other factors such as processing methodology and surface

50   topography, makes it difficult to measure small changes for much of the word's ice covered

51   regions (Arthern et al., 2001; Gray et al., 2015; Nilsson et al., 2015b).

52   The mitigation of these effects in the processing of radar altimetry data is required for

53   improved accuracy of derived temporal and spatial changes in surface elevation of glaciers and

54   ice sheets. Several studies have proposed different approaches to assess these effects and

55   improve the retrieval process of surface elevation and elevation changes from radar altimetry

56   data. These include different approaches to waveform retracking (Davis, 1993, 1997; Gray et

57   al., 2015; Helm et al., 2014) and empirical corrections to the estimated surface elevation

58   changes (Davis and Ferguson, 2004; Flament and Rémy, 2012; Sørensen et al., 2015;

59   Wingham et al., 2006b; Zwally et al., 2005, 2011). Relatively little work has been done to assess

60   methods for improving elevation and elevation changes derived from ESA's CryoSat-2 data

61   (Abulaitijiang et al., 2015; Gray et al., 2013, 2015; Helm et al., 2014).

62   Here we conduct a thorough analysis of CryoSat-2 SIN and LRM waveform retracking,

63   filtering and processing methodologies to design an optimal processing methodology for

64   CryoSat-2 elevation retrieval over both smooth and complex ice-covered terrain. We then

65   analyze two different approaches to determining surface elevation and volume changes from

66   the scattered CryoSat-2 elevation retrievals. The overarching goal of this work is to develop

67   robust and accurate elevation retrieval algorithms that are less sensitive to changes in surface

68   and sub-surface scattering properties.

69   The new processing scheme is applied to estimate elevation and volume changes of the

70   Greenland Ice Sheet for the period January 2011 to January 2015, using two independent

71   methods to characterize the robustness of the results due to methodology. The results are

72   compared to change estimates obtained from the ESA L2 Baseline-B surface elevation product

73   (Bouzniac et al., 2014), high accuracy airborne data from NASA IceBridge airborne topographic

74   mapper and seasonal height amplitudes estimated from Ice, Cloud, and Elevation Satellite

75   (ICESat) data.

76   ## 2 - Surface elevations from CryoSat-2

77   ## 2.1 - Low Resolution Mode (LRM)

78   The LRM mode is used over the interior parts of the ice sheet, which mostly consist of low

79   sloping terrain. Here, SIRAL operates as a conventional pulse limited radar system with a

80   transmission frequency of 13.6 GHz (Ku-band) and has Pulse-Limited Footprint (PLF) radius of

81   approximately 1.5 km and a beam-limited footprint (BLF) radius of approximately 7.5 km over

82   flat terrain (Bouzinac, 2014). The gentle terrain allows for accurate mapping of the surface

83   elevation of the ice sheet down to decimeter-level (Brenner et al., 2007). Within the LRM

84   waveform we define the location of the surface from the leading edge of the waveform, based

85   on a fraction of the maximum amplitude of the received power. This approach is commonly

86   referred to as a threshold retracker. Following Davis et al. (1997) we use 20% threshold to

87   define the location of the surface. Davis et al. (1997) argued that a 20% threshold represents

88   the best compromise between waveforms that are entirely dominated by either volume or

89   surface scattering, making it suitable for obtaining estimates of surface elevation for most parts

90   of the Greenland Ice Sheet.

91   The CryoSat-2 LRM radar waveforms suffer from measurement noise, in the form of

92   speckle noise. Furthermore, over the steeper parts of the LRM-area the range gate tracking-

93   loop can loose track of the surface, producing non-usable waveforms. To remove bad or loss of

94   track waveforms the radar waveform (20 Hz) is first filtered using a zero-phase low pass filter to

95   reduce speckle noise on a line-by-line basis. The signal-to-noise-ratio (SNR) of the waveform is

96   then estimated and if the SNR < 0.5 dB the waveform is rejected. The SNR threshold was

97   empirically chosen to obtain a good trade-off between the quality of the measurements and

98   sampling.

99   Before the waveform can be retracked the first surface return (first major peak) is

100   identified within the range gate window. A copy of the waveform is heavily smoothed to remove

101   small-scale surface roughness signals, keeping the overall surface signal intact. The range gate

102   index of the first peak from the copy is then used to extract the leading edge of the original low

103   pass filtered waveform. Only leading edges with a peak index above 20 are used in the

104   retracking, as peaks before or after that can indicate troublesome surface ranging. The

105   extracted leading edge is then oversampled by a factor of 100 (c.f. (Gray et al., 2013; Helm et

106   al., 2014), and the range R between the surface and satellite is determined based on the 20%

107   threshold computed according to Davis et al. (1997). The range is then corrected for several

108   atmospheric and geophysical effects relevant to land ice studies according to Bouzinac (2014).

109   The surface elevation H of the topography, relative to the WGS84 ellipsoid, is estimated as $H =$

110     $A - R$, where A is the altitude of the satellite.

111   The measured surface return over a sloping surface does not originate from the

112   satellites nadir location, but from the "Point Of Closest Approach" (POCA) to the spacecraft

113   (Brenner et al., 1983). These off-nadir returns can introduce a large range bias to the surface,

114   depending on the magnitude of surface slope, ranging from 0-120 m (Brenner et al., 1983) as

115   the measured surface height is mapped to an erroneous position (i.e. the nadir position). To

116   mitigate the effect of this error we correct the measured range and location to the POCA point

117   using an a-prior DEM, following the approach of Bamber (1994). In contrast to previous studies

118   we account also for the local surface curvature, as Remy et al. (1989) showed that accounting

119   for surface curvature in addition to surface slope significantly improve results. The surface

120   slope, aspect and curvature are estimated from an a priori DEM. The GIMP elevation model

121   (Howat et al., 2014) was used to derive surface parameters for the slope-induced error

122   correction in the LRM mode. The DEM was resampled to 2 km resolution, using bilinear

123 interpolation, prior to parameter estimation, which provided the lowest root-mean-square-error

124 and further corresponds to the pulse-limited footprint of the LRM mode.

2.2 - Interferometric Synthetic Aperture Radar Mode (SIN)

126 The SIN mode is used over the marginal areas of the ice sheets and other smaller glaciated

127 areas. In these areas the SIRAL altimeter operates as a Doppler/Delay radar system (Raney,

128 1998). The Doppler/Delay radar allows for higher along-track resolution compared to

129 conventional altimetry, resulting in 350 m resolution in along track and 1500 m across track. In

130 ordinary SAR operation only the amplitude of the radar echo is measured and the phase content

131 is discarded or ignored. With the inclusion of a second antenna on CryoSat-2, interferometric

132 SAR can also be performed. The difference in path length between the POCA and the individual

133 antennas introduce a phase shift between the two retrieved signals that can be related to the

134 angle of arrival (look angle). The look angle can in turn be used to resolve the across track

135 (across antenna) location of the echo.

136 Multi-look processing is applied to ESA's L1B waveform product (Bouzinac, 2014) to

137 reduce the noise in the SIN waveform but it is still affected by speckle-noise, as is the case for

138 the LRM waveforms. To mitigate this effect, and to help identify the leading edge of the first

139 return, we apply speckle reduction filtering and leading edge extraction of the SIN waveforms in

140 the same way as for the LRM processing with minor changes due to differences in range gate

141 resolution. In this case, compared to the LRM retracking algorithm, only leading edges with a

142 peak index in the range of 100-350 are used for retracking the radar waveform (P_w).

143 The estimated coherence C of the multi-looked waveforms is then filtered in two stages;

144 (i) all coherence measures larger than one is set to zeros (coherence values larger than one

145 exists in the L1B product due to unknown reasons). (ii) The coherence array, as a function of

146 range, is filtered using a 2D 5x5 Wiener filter to remove high frequency noise. The filtering of the

147   waveform and the coherence is applied to remove noise in the recreation of the interferogram,

148   discussed below.

149   The measured differential phase ϕ of the return signal is affected by phase ambiguities;

150   a sudden shift of 2π in the measured phase. To reduce phase noise and aid the phase, an

151   unwrapping of the radar interferogram I is performed according to Gray et al. (2013):

152                                    $$I = P_w \cdot C \cdot e^{-i\phi}$$ (1)

153   The interferogram is then filtered using a wavelet-based de-noising technique, where the real

154   and imaginary parts of the interferogram are filtered separately. The unwrapping of the

155   interferogram allows for indirect filtering of the phase, without being affected by the phase-

156   ambiguities. Phase filtering is an important consideration as it has a direct affect on accuracy of

157   the position of the ground echo. We selected a bi-orthogonal as the mother wavelet to produce

158   the wavelet coefficients decomposed into three levels. Soft thresholding was applied to detail

159   coefficients, using a heuristic threshold rule to remove noise at every level. This was done on a

160   line-by-line basis. The final filtered differential phase was then recovered by:

161                                    $$\phi_f = Re\{I_f\} + Im\{I_f\}$$ (2)

162   To resolve the phase ambiguities the filtered phase measurements require unwrapping. The

163   phase unwrapping is done on a line-by-line basis in two directions starting from the center of

164   gravity of the waveform (Wingham et al., 1986).

165   The return power distribution of a Doppler/Delay radar system shows an important

166   distinction from those from conventional pulse-limited radar systems. Here, the point

167   corresponding to the mean surface is not located at the half-power point on the leading edge,

168   but rather closer to the maximum (Wingham et al., 2006a). Therefore a new retracker has been

169   developed, closely related to the one used in Gray et al. (2013), to allow for adaptive retracking

170   of the upper parts of the leading edge of the SAR waveform. The algorithm follows the main

171   concept of the threshold retracker, developed by Davis (1997), but instead of a pre-defined

172 threshold it tracks the maximum gradient of the leading edge of the oversampled waveform. We

173 refer to this approach as that "Leading-edge Maximum Gradient retracker" (LMG).

174   The surface returns are geolocated using the across track look-angle θ estimated from

175 the differential phase at the retracking point according to (Wingham et al., 2006a). This, in

176 combination with the viewing geometry, is used to define the location of the surface return on

177 the ground using basic across track interferometric principles. We correct θ for the

178 interferometer surface slope error by applying the look-angle scaling factor estimated in (Galin

179 et al., 2013).

180   The along-track differential phase estimate, interpolated to the retracking point, is

181 affected by phase ambiguities not corrected for during the phase unwrapping procedure. To

182 reduce residual phase ambiguities an a priori DEM (GIMP) is used to extract the DEM surface,

183 resampled to 500 m resolution (corresponding roughly to the along-track sampling), elevations

184 at the nadir and echolocation using bilinear interpolation. Over a sloping surface the surface

185 return should always come from a position upslope from the nadir point. Therefore the following

186 relation must hold where ($H_{echo} > H_{nadir}$) or for a more practical application ($H_{echo} - H_{nadir}$) > ε,

187 where ε is the uncertainty of the DEM used. If this relation is violated 2π is added or subtracted

188 to the individual along-track phase estimate, depending on the sign.

189   A final step is applied to correct for any lingering phase ambiguities not corrected by the

190 a priori DEM. This step uses the assumption that the along-track phase should follow a

191 consistent pattern over most part of the satellite ground track. Hence, any large discrepancies

192 from the overall pattern of the along-track phase would indicate an ambiguity. The ambiguity is

193 detected by computing the residuals of the along-track phase by removing a smoothed version

194 of the differential phase. If any of the residuals have a magnitude larger than π it is considered

195 ambiguous and thus corrected by adding or subtracting 2π.

196   3 - Surface elevation changes from CryoSat-2

197   3.1 – Surface fit method

198   The surface-fitting method is based on fitting a linear model to the elevations as a function of

199   time and space inside a search radius of 1 km (e.g., Howat et al., 2008; Moholdt et al., 2010;

200   Sørensen et al., 2011; Wouters et al., 2015). The linear model consists of a time-invariant

201   (static) bi-quadratic surface model to account for variable topography inside the search radius

202   and time-variant part used to extract the temporal change in elevation. The model consists of a

203   total of 7-parameter whereof six of the parameters (a-coefficients) describe the bi-quadratic

204   surface modeling function, *dh/dt* the linear elevation change rate, *t* time in decimal years, t_0 the

205   mean time inside the footprint and ε the residuals from the linear regression.

206    $$h(x,y,t) = a_0 + a_1 x + a_2 y + a_3 xy + a_4 x^2 + a_5 y^2 + \frac{\partial h}{\partial t}(t - t_0) + \varepsilon \qquad (3)$$

207   The algorithm estimates the elevation change at every echolocation (or grid-node if desired) in

208   the data set. In each solution the signal amplitude and phase are also estimated by fitting a

209   seasonal signal model to the surface-fit elevation residuals, according to:

210    $$\Delta h(t) = s_0 \cos(wt) + s_1 \sin(wt) + \varepsilon \qquad (4)$$

211   where *Δh* is the elevation residuals estimated from the plan-fit model, $s_{0,1}$ are the model

212   coefficients and t the time. The amplitude *A* is then defined as $A = \sqrt{s_0^2 + s_1^2}$ and the phase *P* as

213    $P = \tan^{-1}\left(\frac{s_1}{s_0}\right)$.

214   To remove outliers an iterative 3σ-filter is used in the full model solution, i.e. the

215   topography, trend and seasonal signal are removed, using a maximum of 5-iterations. For each

216   iteration residuals (full-model) with an absolute value larger than 10 m are removed, as

217   seasonal changes larger than 10 m are not expected (Moholdt et al., 2010; Qi and Braun,

218   2013). The data inside the 1 km cap is weighted according to their distance from the estimation

219   point according to:

220
$$W = \frac{1}{\left(1+\left[\frac{d}{\rho}\right]^2\right)}$$
(5)

221 where W is the estimated weight, d the distance and ρ the correlation or resolution parameter

222 set to 500 m. The weighting allows the solution to better reflect local signal dynamics at the

223 prediction point.

224

225   Local elevation time-series are further computed from the elevation residuals and

226 elevation trend from each solution, according to:

227
$$h(x,y,t) = (t - t_0) \cdot \frac{\partial h}{\partial t} + \varepsilon$$
(6)

228 where t is the time epochs inside the search cap, t_0 is the mean time of t, dh/dt is the estimated

229 elevation change rate and ε is the elevation residual at each time epoch.

230   The elevation changes estimated from the surface-fitting method are then culled to

231 remove outliers before spatial gridding. Elevation changes with a regression error larger than 15

232 m a^{-1} are removed. The resulting surface elevations are binned at 5-km resolution for outlier

233 editing purposes. For each cell the local spatial trend is modeled as a bilinear surface, and

234 removed. The residuals are then edited using an iterative 3σ filter until the RMS converges to

235 2%.

236 3.2 – Crossover method

237 The crossover method is used to derive the surface elevations at the intersection point between

238 an ascending and descending satellite ground track separated in time (Brenner et al., 2007;

239 Khvorostovsky, 2012; Zwally et al., 1989). The surface elevations and times are then estimated

240 at the crossover location for each track by linear interpolation of the two closest data points for

241 each ascending and descending track. The crossover height difference is then estimated by

242 taking the height difference between the two tracks according to:

243
$$\Delta h = h_2 - h_1 + \varepsilon \tag{7}$$

244 were h_1 and h_2 are the surface heights at the crossover location at time epoch t_1 and t_2,

245 respectively, and E is the random measurement error, including orbital, range and retracking

246 errors.

247 This approach produces crossover height differences with scattered time-epochs

248 ranging from 0-4 years. CryoSat-2 has a 369-day repeat orbit configuration with a 30-day sub-

249 cycle meaning that each crossover location will be revisited every 369 days and surrounding

250 area every 30 days. This produces annual and sub-annual crossover difference around each

251 crossover location. This fact is used to produce elevation change rates by incorporating all

252 multi-temporal crossover difference within a neighborhood of 2.5-km around each crossover

253 location. The elevation change is then estimated using the same procedure described for the

254 surface-fit method, except that a bilinear model is used to remove any spatial trends in the

255 topography of the crossover elevations according to:

256
$$dh(x, y, t) = a_1 x + a_2 y + \frac{\partial h}{\partial t}(t - t_0) \tag{8}$$

257 where dh is the crossover height difference, t the time, t_0 is the mean reference time inside the

258 footprint, a_1 and a_2 the across and along-track slope and dh/dt the elevation change rate. This

259 produces elevation changes comparable in time and in spatial coverage with the surface-fit

260 method. The same outlier editing schemes is applied to the crossover elevation change rates as

261 for the surface-fit method.

3.3 - Gridding of sparse elevation and elevation change data

263 The gridding is done in a polar-stereographic projection with a latitude of origin at 70°N, central

264 longitude of 45°W and origin at the North Pole. The projection is referenced against the WGS-

265 84 ellipsoid and the grid-resolution. The observations derived from the surface-fit and crossover

266 method are gridded at a resolution of 1x1-km, due to the high spatial sampling.

267   The method of Least Squares Collocation (LSC), described in Herzfeld (1992) is used to

268   grid the observations onto a regular grid. LSC is similar to Kriging and allows for optimal

269   interpolation and merging of data with different accuracies, using their inherent covariance

270   structure. The LSC-algorithm uses the 25 closest data points in 8-quadrants surrounding the

271   prediction point to reduce spatial biasing. The prediction equation consists of two terms where

272   the first term is the actual prediction term and the second term accounts for the non-stationary

273   part of the data, as described by:

$$\hat{s} = C_{sz}(C_{zz} + N)^{-1}z + \left(1 - \sum (C_{sz}(C_{zz} + N)^{-1})\right)m(z) \tag{9}$$

274   were $C_{\hat{s}z}$ is the cross-covariance, C_{zz} is the auto-covariance, N the diagonal noise-matrix

275   consisting of the a priori RMS-error and $m(z)$ is the median value of the observations inside the

276   search neighborhood.

277   The covariance of the data inside the local neighborhood is modeled as a function of

278   distance away from the prediction point using a third-order Gauss-Markov model described

279   below.

$$C(r) = C_0 \left(1 + \frac{r}{\alpha} - \frac{r^2}{2\alpha^2}\right) e^{\left(-\frac{r}{\alpha}\right)} \tag{10}$$

281   where r is the separation distance, C_0 the local data variance and α is a scaling factor estimated

282   from the correlation length.

283   LSC interpolation provides a RMS-error for each prediction point estimated from the

284   modeled covariance of the data according to:

$$C_{\hat{s}} = C_0 - C_{sz}(C_{zz} + N)^{-1}C_{sz}^{T} \tag{11}$$

285   where the RMSE of the prediction equals to $\sigma_{\hat{s}} = (C_{\hat{s}})^{1/2}$ and where $C_{sz}{}^T$ is the transposed cross-

286   covariance matrix.

287   The elevation changes estimated from the surface-fit and crossover methods are

288   interpolated to a regular grid using their a priori error estimated from the LSC scheme. To avoid

289   unrealistically small errors, common in the regression errors estimated over flat terrain, a

290   minimum error threshold is applied. Error values smaller than a specific threshold are set to the

291   threshold value. The threshold value is representative of the overall precision of the elevation

292   changes over flat terrain and is set to 0.2 m a^{-1}. The data are then gridded using a 75 km

293   correlation length determined from the comparison of CryoSat-2 elevation to airborne

294   measurements (Section 5).

295   The LSC algorithm is also used to generate a DEM based on the surface elevations

296   generated from the surface-fitting algorithm. The surface elevations generated from the surface-

297   fit were used as input to the gridding-algorithm. The use of surface elevations from the surface-

298   fit provides several advantages compared to the raw observations as they: provide an almost

299   equal number of observations as the raw data, have been screened for gross outliers, have

300   been low-pass filtered using the 1-km search radius, and are all reference to roughly the same

301   time epoch. Further the RMSE error generated from the surface-fit estimated surface height can

302   be used as an a priori error for the LSC gridding procedure.

303   The DEM is generated using the same approach as for the surface elevation changes,

304   as described previously in the section. Before the gridding procedure is applied elevations $H < 0$

305   and $H > 3350$ m are removed from the data set. Further, elevations with a standard error larger

306   than 30 m are also removed. The elevations are binned spatially into a resolution of 1000 m and

307   inside each cell the local surface trend is removed by fitting of a planar surface, and an iterative

308   3σ filter is applied to the residuals to remove outliers.

309   4 - Surface elevations and elevation changes from ICESat

310   To assess basin-scale patterns of elevation change we compare elevation changes from

311   CryoSat-2 data to elevation changes derived from Ice, Cloud, and Elevation Satellite (ICESat)

312   data. Here we use release 33 (GLA06) data collected over the 2003-2009 period. The ICESat

313   surface heights were used to generate surface elevation changes and seasonal parameters

314   according to method M3 in Sørensen et al. (2011). The derived elevation changes were

315   corrected for the G-C offset (Borsa et al., 2014). Valid elevation retrievals were selected

316   according to Nilsson et al. (2015b). The ICESat elevation, seasonal amplitude and phase, are

317   then used for comparison with CryoSat-2 and to build continuous time series using the surface

318   fit method described in Section 3.1. For the purpose of this study no correction for the inter-

319   campaign bias was applied, as this is still an active area of investigation.

320   5 -Validation

321   Elevation and elevation change results were generated for the entire Greenland Ice Sheet using

322   CryoSat-2 data collected between Jan-2011 and Jan-2015 using the methodology presented in

323   (Sections 2-3) (JPL product) and by applying the methods of (Section 3) to ESA's CryoSat-2 L2

324   elevation products (ESA product). Surface elevations and elevation changes were validated

325   against airborne data sets obtained from NASA's Operation Ice-Bridge Airborne Topographic

326   Mapper (ATM), obtained from the "National Snow & Ice Data Center" (NSIDC) in the form of the

327   ILATM2 product. The generated elevation product has a resolution of 80 m, with a 40 m spacing

328   along-track. This mission produces both elevation and elevation changes with reported vertical

329   accuracy of ~10 cm and temporal accuracy in the cm-level (Krabill et al., 2002).

330   The derived surface elevations from CryoSat-2 are differenced against ATM surface

331   elevations within 50 m of each ATM locations. One month of CryoSat-2 data consistent in time

332   with the ATM elevations are used for the validation to avoid biases due to temporal sampling

333   and to obtain sufficient sample size. A total of four years of campaign data are used for the

334   validation of the surface elevations (2011-2014). The residuals are edited using an iterative 3σ

335   filter to remove outliers. The accuracy and precision is estimated as the mean and standard

336   deviation of the differences, respectively. The residual distribution is further binned according to

337   surface slope estimated from the GIMP DEM (Howat et al., 2014) resampled to 500 m. The

338   sensitivity to surface slope (slope error) can be identified in the standard deviation of the binned

339   residuals and can be used to judge the quality of the produced surface elevation and elevation

340   changes, while the binned-average for the elevations can be used to determine radar-signal

341   penetration depth.

342   Surface elevation change rates estimated from three different time-periods (2012-2014,

343   2011-2013 and 2011-2014) of overlapping ATM observations (Krabill, 2014) are used to validate

344   the surface elevation changes estimated from the CryoSat-2 data. The same validation

345   methodology applied to surface elevations is applied to surface elevation changes, with a few

346   minor modifications. First the search radius is increased to 175 m to make it conform to the ATM

347   elevation change resolution of 250 m, as this search radius encloses the entire ATM grid cell.

348   Secondly the estimated mean and standard deviation are multiplied with the individual time-

349   intervals of the validation data sets to make the errors comparable, as they differ in time span.

350   For the surface-fit and crossover methods, near-coincident elevation change rates were

351   compared with ATM rates (e.g., April-2011 to April-2014). This provided three validation data

352   sets for the surface-fit method, due to its high spatial coverage. However, only the 2011-2014-

353   validation data set could be used for the crossover method, due to the lower spatial sampling of

354   the crossovers.

355   The overall accuracy and precision for both the surface elevation and elevations

356   changes are then estimated by taking the weighted mean, using the number of observations as

357   weights, for each data set giving an average error for each measurement mode, as seen in

358   Table-2. The weighted average errors for each mode and method have been summarized in

359   Table-1 and Table-2 for both the ESA's and our solutions, where the values for the individual

360   campaigns can be found in the Supplementary material.

361   The estimated surface elevation changes from the two independent methods were

362   validated separately using near-coincident ATM data. The statistics of the elevation change

363   validation have been summarized in Table-2 for each method independently for the two modes

364   of instrument operation. We find the lowest RMSE errors for the surface-fit method, followed by

365 the crossover method. This differs from the findings of Moholdt et al. (2010) who found lower

366 intrinsic errors for the crossover method, compared to the surface-fit method when applied to

367 ICESat data. The larger search radius used for our application of the crossover method most

368 likely explains the difference in findings between the two studies. Further, we find that the

369 surface-fit method provides the largest reduction in RMSE for the JPL product, corresponding to

370 40% and 55% for the SIN and LRM-mode, respectively.

371 The correlation length used to derive the number of un-correlated grid-cells, which is

372 used to estimate the standard error, was determined from a semi-variogram analysis of the

373 elevation change residuals from CryoSat-2 minus ATM using the data from the surface-fit

374 method. The comparison was done for each mode separately for all the individual campaigns

375 and multiplied with the their individual time span. The semi-variogram was then computed from

376 all the time-invariant residuals, to maximize the spatial coverage, for each mode. Analysis of the

377 semi-variogram showed approximate correlation lengths of 100 and 75 km for the SIN and

378 LRM-mode respectively. These correlation lengths are inside the range of the ones found by

379 Sørensen et al. (2011) for their analysis of ICESat data, which was found to be between 50-150

380 km.

381 The main goal of this study is not to derive or compare different types of DEM's.

382 However, to gain insight into the overall quality of our CryoSat-2 derived DEM (referred to as

383 JPL) we compare it to three other DEM's derived from other data sets Firstly, we compare it to

384 a DEM derived from ESA CryoSat-2 L2 data (referred to as ESA) gridded in the same manner

385 as our DEM (Section 3.3). Secondly we compare it to a DEM from Helm et al. (2014), also

386 based on CryoSat-2 data from 2011-2014 (referred to as AWI). Thirdly, we compare to a DEM

387 from Howat et al. (2014) (which was used to derive topographical parameters and corrections

388 for the JPL CryoSat-2 data), based on photogrammetry and altimetry data from the mid 1990's

389 to 2010 (depending on data source) co-registered to ICESat elevation data from 2003-2009

390 (referred to as GIMP).

391   These data sets were then compared to IceBridge ATM elevations, spanning the four

392   different campaigns previously used for validation of the CryoSat-2 elevations. The DEM

393   elevation was estimated at each ATM location, using bilinear interpolation, and the elevation

394   difference computed as (DEM-ATM). No attempt was made to account for differences in DEM

395   and ATM epochs. The estimation of the errors of the DEM was determined in the same way as

396   for the individual CryoSat-2 surface heights. The results of the comparison have been

397   summarized in Table-3, as the weighted average of the different campaigns. The values from

398   each individual campaign can be found in the supplementary material.

399   Analyzing the overall RMSE we find that the AWI produces the lowest RMSE, followed

400   by JPL, ESA and GIMP, due to AWI's lower standard deviation. However, the best accuracy is

401   obtained by the JPL DEM, which shows the lowest elevation bias of all DEM's. The ESA derived

402   DEM shows a slightly better standard deviation than the JPL DEM, which can be explained by

403   higher data density in the marginal areas for the ESA data. The difference in density is due to

404   the SNR rejection criterion applied in our elevation processing. The lower standard deviation in

405   the AWI product is mostly likely due the use of lower resolution topography in many of the high

406   relief areas in the 1 km elevation model, producing a smoother estimate of the surface. The

407   GIMP data set showed higher degrees of impulse noise than the other products, explaining the

408   higher observed standard deviation. This impulse noise is attributed to that local elevation

409   change rate, which was not accounted for in the creation of the DEM (Howat et al., 2014).

410   Overall we find that the JPL DEM provides a suitable compromise between resolving of local

411   detail and the minimization of bias. Further, modification to the SNR filtering criteria will likely

412   lead to additional improvements in the DEM.

413   To determine the effect of retracking on the accuracy and precision of the measured

414   surface heights from CryoSat-2 several tests was performed over different parts of Greenland

415   for both modes. Following the approach of Davis (1997) the accuracy (mean) and precision

416   (standard deviation) was computed as a function of leading edge threshold (in percent). This

417   computation was performed using a standard leading-edge threshold retracker, referred from

418   now on as LTH, for both the LRM and SIN mode independently. The validation was performed

419   in the same manner as described in Section 5, where ATM elevations from 2013 was used as

420   the surface reference.

421   For the LRM mode data from April 2013 from the northern parts of Greenland, spanning

422   the region 75-81°N and 54-44°W around the North Greenland Eemian Ice Drilling camp

423   (NEEM), was used to calculate height residuals for the different thresholds. This produced

424   approximately 1000 comparison locations, which was used to calculate statistics. The same

425   procedure was performed over Jakobshavn Isbræ, using the same time span, to calculate

426   statistics for the SIN-mode providing roughly 2500 comparison locations.

427   The results of this analysis, summarized in Figure-2, show that for the LRM-mode the

428   precision (as a function of threshold) follows the same behavior as observed by Davis (1997),

429   with a decrease of precision following increasing retracking threshold. However, the most

430   notable finding was the observed inverse relationship in precision for the SIN-mode compared

431   to LRM. For LTH-algorithm, in the SIN-mode, we observe a clear increase in precision as the

432   retracking threshold increases, seen in Figure-2, stabilizing around 30-40%.

433   Analyzing the accuracy derived from the different thresholds a clear difference in apparent

434   penetration depth of the radar signal can be observed for the two modes. For the SIN-mode,

435   below 40%, a positive bias is observed indicating that retracker produces elevations larger than

436   the corresponding airborne measured heights. For thresholds larger than 40% surface

437   penetration of the signal is observed which are in general closer to the surface compared to the

438   LRM-mode. We attribute this to differences in the near-surface density structure covered by the

439   two modes.

440   In general we conclude that for the LRM-mode applying low retracking thresholds (0-

441   30%) reduces the magnitude of the apparent surface penetration bias and provides higher

442   precision compared to higher thresholds. Therefore, a threshold of ~20% of the leading edge is

443   suggested for retracking surface elevations for the LRM-mode, which was also previously

444   suggested by Davis (1997) and Helm et al. (2014). However, for the SIN mode a threshold

445   below 40% is not recommended, as this produces a clear positive elevation bias and poor

446   precision, as seen in Figure-2. Analyzing the difference between the LTH and the adaptive LMG

447   algorithm, used in the SIN-mode, we find that the LMG algorithm produces superior results in

448   precision compared to the standard LTH-algorithm. Comparing the adaptive solution from LMG

449   to the optimum threshold found by the LTH-algorithm, we find a comparable magnitude of the

450   elevation bias and a 32% improvement in precision, with an overall 27% reduction in RMSE,

451   using the LMG-retracker. From this comparison between the two-retracker algorithms we

452   recommend the use of the adaptive threshold approach (LMG), as it produces an elevation

453   repeatability that exceeds that of the standard threshold retracker (LTH) and provides a low

454   penetration bias.

455   A case study was also performed to determine the different processing steps effects on

456   the quality of the retrieved elevations. For this purpose the Barnes ice cap, on Baffin Island in

457   the Canadian Arctic, was chosen due to its small size, excellent validation coverage and due to

458   that it consist mostly of super-imposed ice (reducing radar signal penetration). The ice cap saw

459   a major IceBridge ATM campaign in 2011 providing a large number of flight tracks (spanning in

460   both North-South and East-West directions) suitable for validating CryoSat-2 data. The result of

461   this case study, which is detailed in supplementary material (i.e. Table-S1) shows that the

462   filtering of the differential phase has the highest impact on the overall accuracy of the

463   observation, reducing the RMSE by 12%, followed by the ambiguity correction. This shows the

464   importance of these steps, as they can have important implications for the overall quality of the

465   retrieved elevations. This is especially true in high relief areas where small changes in the look

466   angle, or an introduced phase ambiguity, can produce large elevation errors ranging from 0-100

467   m in elevation (Brenner et al., 1983).

468

469   6 - Error analysis

470   To compute volume change errors for the two methods we divide the error budget into two main

471   components (1) the observational standard error (ε_{obs}) and the interpolation standard error (ε_{int}).

472   The observational error budget is estimated using the root-mean-square error (RMSE) of the

473   difference between CryoSat-2 and airborne elevation change differences, as described in

474   Section 5. The RMSE is estimated separately from the two different modes, with the total

475   volume change error (ε_{vol}) being computed as the RSS of the standard elevation change error of

476   the two modes and their corresponding area, according to:

$$\varepsilon_{vol} = \sqrt{(\varepsilon_{lrm} \, A_{lrm})^2 + (\varepsilon_{sin} \, A_{sin})^2} \qquad (12)$$

478   were A_{lrm} and A_{sin} are the areas covered by each mode. The ε_{lrm} and ε_{sin} are the standard

479   elevation change errors of the LRM and SIN computed from the airborne validation data sets.

480   The observational elevation change error is estimated from the residual elevation

481   change differences in Table-2 for the two methods. The RMSE from the LRM/SIN errors are

482   computed using Gaussian error propagation producing an observational elevation change error

483   (σ_{obs}). For the surface-fit and the crossover method the interpolation error is estimated as the

484   RMS of the LSC uncertainty grid, defined as (σ_{int}). The final elevation change error is then

485   estimated by combing the two error sources using RSS according to:

$$\varepsilon_{mode} = \varepsilon_{dh/dt} = \sqrt{(\varepsilon_{obs})^2 + (\varepsilon_{int})^2} = \sqrt{\left(\frac{\sigma_{obs}}{\sqrt{N}}\right)^2 + \left(\frac{\sigma_{int}}{\sqrt{N}}\right)^2} \qquad (13)$$

487   Here, N is the number of uncorrelated grid-cells estimated from empirical semi-variogram

488   analysis of the CryoSat-2 and airborne elevation change differences, and estimated according

489   to:

$$N = \frac{A_{mode}}{\rho_{mode}^2} \qquad (14)$$

490   were A_{mode} is the total area of the Greenland Ice sheet ($\sim 1.7 \times 10^6$ km^2) and the correlation length

491   ρ_{mode} of 75 and 100 km for the LRM and SIN mode respectively.

492   7 – Results

493   7.1 – Surface elevations compared to ATM

494   The measured surface elevations from the two CryoSat-2 products (JPL vs. ESA)

495   showed large differences in both accuracy and precision of the elevation measurements, as

496   seen in Table-1. The average accuracy and precision for the LRM-mode from the two products

497   showed values of 0.00 ± 0.43 m and -1.06 ± 0.89 m for the JPL and ESA products respectively.

498   This corresponds to an average reduction in RMSE of 68% for the JPL product compared to the

499   ESA LRM L2 data. Further, our product shows a lower residual slope error (seen in Figure-1c

500   below ~0.5°) indicating a lower sensitivity to the degradation of performance as the surface

501   slope increases.

502   Surface elevations generated from the SIN-mode showed the same type of improvement

503   as for the LRM-mode. Here, an average accuracy and precision was found to be -0.52 ± 0.58 m

504   and -0.90 ± 1.05 m for the JPL and ESA SIN elevation products respectively. This further

505   corresponds to a reduction in the average RMSE of 27% for the JPL product compared to the

506   ESA product. For the SIN-mode the JPL processing produces a slightly lower residual slope

507   error, compared to the ESA processor (seen in Figure-1c above ~0.5°)

508   Larger improvements can be observed if separating the RMSE into its mean and

509   standard deviation, corresponding to the accuracy and precision of the measurements. Using

510   these definitions the analysis found that there is a 45% and 52% increase in precision for the

511   SIN and LRM mode respectively, compared to the ESA L2 product, and a 42% and 99%

512   improvement in accuracy for the respective modes.

513   The implementation of the LMG SIN retracking algorithm was found to reduce noise in

514   the retrieved surface elevations compared to conventional threshold retracking. Though roughly

515   comparable in accuracy, the LMG shows overall higher precision over all comparable leading

516   edge thresholds. The adaptive nature of the algorithm provides improved estimates of surface

517   elevation and a good trade-off between accuracy and precision.

518   The 20% threshold retracker implemented in the LRM-mode was also found to provide

519   improved estimates of surface elevation (both in accuracy and precision) compared to the

520   model-based ESA-L2 retracker. Further, it also showed lower sensitivity to the 2012 melt event,

521   due to the lower threshold used on the leading edge of the waveform.

522   ## 7.2 – Surface elevation changes compared to ATM

523   The estimated surface elevation changes generated from the surface-fit method also

524   showed improvement in the estimated accuracy and precision, as seen in Table-2. Here, an

525   overall improvement in RMSE of 55% and 40% in the LRM and SIN mode, respectively, was

526   found when comparing against ESA L2 generated elevation changes from the same method.

527   The average accuracy and precision, compared to ATM generated elevation changes, was

528   found to be 0.11 ± 0.67 m (LRM) and 0.30 ± 0.58 m (SIN) for the JPL derived changes. This

529   compared to 0.25 ± 1.51 m (LRM) and 0.34 ± 1.06 m (SIN) for the ESA derived changes. This

530   corresponds to an increase in elevation change accuracy of 56% and 12% for the LRM and

531   SIN-mode, respectively, for the JPL product compared to ESA L2 elevation changes. The

532   estimated elevation changes also show an increase in precisions for the JPL product of 56%

533   and 45% for the LRM and SIN-mode, respectively, compared to its ESA counterpart.

534   The estimated elevation changes of the Greenland Ice Sheet, excluding the peripheral

535   glaciers, over the period January 2011 to January 2015 show significant differences between

536   products (JPL and ESA) in both spatial patterns and the total magnitude (Figures 3 & 4). The

537   estimated volume change rate from the surface-fit method is -289 ± 20 $km^3 a^{-1}$ for the JPL-

538   product and -224 ± 38 $km^3 a^{-1}$ for the ESA-product with a mean difference of 65 $km^3 a^{-1}$. The

539   surface-fit and crossover-method produced on the order of ~20 million and ~2.5 million usable

540   elevation changes, respectively, providing high spatial sampling. Due to the constraint put into

541   the JPL processor the ESA L2 data produced slightly more surface-fit observations (~10%), as

542   more surface elevations were accepted.

543   The ESA product produces a more positive elevation change pattern, which can be

544   attributed to the 2012 melt event that introduced a large positive bias with a magnitude of ~0.5

545   m (Nilsson et al., 2015a). Larger differences in the marginal areas for the surface-fit methods

546   are also observed. The positive signal detected in the interior of the ESA surface-fit-solution can

547   also be found in the basin time series, correlating well with the timing of the summer of 2012

548   melt event, which for example can be seen in the time series in Figure 3. These results are in

549   agreement with earlier work demonstrating the sensitivity of the ESA retracker to the changes in

550   the volume/surface scattering ratio (Nilsson et al., 2015a).

551   We used ICESat and CryoSat-2 derived surface heights to generate time series over

552   three regions in Northeast area of Greenland (Zachariæ Isstrøm, Nioghalvfjerdsfjorden and

553   Storstrømmen glaciers) for comparison purposes. These areas have in recent time shown large

554   and rapid changes, which has been noted by, e.g., Khan et al. (2014). The selected areas were

555   defined using hydrological basins derived by Lewis and Smith (2009), seen in (Figure 6), and

556   were further divided into smaller areas around the termini to highlight performance for areas of

557   rapid change. The ICESat and CryoSat-2 surface heights were then used to generate annual

558   time-series from 2003-2015 using (Equation 6) in the surface fit method. The estimated 12 year

559   time series show overall comparable elevation change rates over both time periods (2003-2009

560   and 2010-2015), especially in the terminus areas, providing confidence that CryoSat-2 can

561   actually monitor changes in these areas.

562

563

564   7.3 – Seasonal phase and amplitude compared to ICESat

565   The amplitude of the seasonal signal (Equation 4) estimated from the surface-fit (SF)

566   method show large differences in both magnitude and spatial variability (Figure 5). For the

567   surface-fit method a difference in amplitude of 54% is observed between the ESA and JPL

568   products, corresponding to area-averaged amplitude of 0.17 m or the JPL product and of 0.37 m

569   for ESA product. The comparison with ICESat derived amplitudes from 2003-2009 estimated in

570   (Sasgen et al., 2012) using the same methodology as used here produced an area-averaged

571   amplitude of 0.13 m, which is in good agreement with the JPL derived amplitude. This

572   agreement is also spatially consistent, as seen in (Figure 5), indicating low sensitivity to

573   seasonal changes in scattering regime of the upper snowpack. The observed difference in

574   amplitude bias, taking ICESat as the true surface amplitude while acknowledging that no inter-

575   campaign bias has been applied and further the differences in epochs, is 0.03 ± 0.13 m for the

576   JPL product and 0.21 ± 0.27 m for the ESA product. The smallest differences are observed at

577   high altitudes above 2000 m a.s.l., where the three data sets show almost constant amplitude of

578   0.1 m (ICE/JPL) and 0.2 m (ICE/ESA), providing a factor of two larger amplitude for the ESA

579   product. Below 2000 m a.s.l., corresponding well to the equilibrium-line-altitude (ELA) of the

580   Greenland Ice Sheet (Poinar et al., 2015), a rapid increase in amplitude is observed for all

581   products. This is especially true for the ESA product, which increases its magnitude by a factor

582   of two.

583   Analyzing the amplitude patterns on a regional drainage basin level (Figure 5c) we find

584   good agreement between JPL CryoSat-2 and ICESat amplitude with ESA data producing

585   consistently larger amplitudes. Regionally, the highest amplitudes can be observed in the SE of

586   Greenland in basins (3,4,5) and are consistent with regional precipitation patterns that show

587   high average precipitation in these areas (Bales et al., 2009; Ettema et al., 2009).

588   The seasonal phase of the peak in amplitude of the seasonal cycle is shown in (Figures 5b and

589   5c) and shows generally good agreement between the two data sets, providing the timing of the

590   maximum of the accumulation signal, before the onset of melt, to the months of June/July for

591   both JPL and ESA CryoSat-2 data sets. The ICESat derived seasonal phase shows a higher

592   dependence on elevation where the maximum of the accumulation signal is found in late May

593   below 2000 m and late July/August above 2000 m in elevation. The ICESat discrepancies from

594   the CryoSat-2 data are found in specific basins. Disagreements between the retrieved phase of

595   the peak amplitude from Cryosat-2 and ICESat data are due to differences in temporal sampling

596   as discussed in more detail in Section 8.

597   7.4 – Volume change

598   The two volume change methods produce consistent results from JPL derived elevation

599   changes, with a difference of around 1 $km^3 a^{-1}$. The spread between volume change methods is

600   larger (50 $km^3 a^{-1}$) when using ESA L2 data. The larger discrepancy can be mostly related to the

601   sensitivity of the various methods to the melt event. The surface-fit method produces the most

602   negative number (least affected by the melt event and has the lowest estimated error) and is

603   therefore taken as the most reliable estimate for both the JPL and ESA solution.

604   Comparing the estimated volume change to other studies using CryoSat-2 we find that

605   the JPL product is less negative than that estimated by Helm et al. (2014): -375 ± 24 $km^3 a^{-1}$.

606   This difference can be attributed to difference in processing methodology and to the different

607   epoch of the data used by Helm et al. (2014) of January 2011 to January 2014. Using the

608   corresponding epoch the JPL data gives a volume change estimate, based on the surface-fit

609   method, of -353 ± 26 $km^3 a^{-1}$, well within the stated uncertainty of Helm et al. (2014).

610   To examine the regional behavior of volume change estimates of the Greenland Ice

611   Sheet, gridded values from the two methods were divided into 8-drainage basins according to

612   Zwally et al. (2012). When analyzing the elevation time-series at the basin scale clear

613   differences can be observed in the annual and inter-annual behaviors (Figure 4). The northern

614   and interior basins (1, 2, 7, 8) all exhibit large differences (Table 4: 0 - 30 $km^3 a^{-1}$) in the

615   estimated volume change rates due to changes in the scattering regime resulting from the 2012

616   melt event. In the majority of the southern basins (4, 5, 6, 7), located in areas with higher

617   precipitation, both products show good agreement in both trends and seasonal amplitude

618   estimated from the surface-fit method.

619   ## 8 - Discussion

620   The CryoSat-2 processing methodology presented here is found to produce accurate and

621   precise measurements of ice sheet elevation and elevation change. The main improvements

622   have been introduced in the SIN processor with the inclusion of a novel type of land ice

623   retracker (LMG), advanced phase filtering and the inclusion of a phase ambiguity correction

624   scheme. This processing approach decreased the RMSE in the surface height retrieval by

625   approximately 27% (45% and 42% improvement in precision and accuracy). This improvement

626   further propagated into the quality of the estimated elevation changes for the SIN-mode, with

627   the same magnitude of improvement (Table-2). The described SIN-processing also generated

628   surface elevations and elevation changes with lower sensitivity to the local surface slope,

629   indicating a higher degree of accuracy in the geolocation and surface range estimation.

630   The SIN processing methodology further includes a phase filtering and phase ambiguity

631   correction scheme. Visual inspections of a large number of tracks have shown more coherent

632   estimation of the surface locations in the JPL product and further the implementation of the

633   phase-ambiguity correction greatly reduced the number of track offsets. It was also noted that a

634   relatively course DEM (~1 km) could be used to resolve phase ambiguities. The detection and

635   correction of phase ambiguities are relatively straightforward and rely mostly on the relative

636   accuracy of the DEM. The implementation of the phase ambiguity correction is particularly

637 important when monitoring smaller ice caps and outlet glaciers, where frequent and large track

638 offsets can bias the estimation of the underlying topography.

639   The new LRM processing methodology focused on optimal retrieval of surface

640 elevations over the interior parts of the ice sheet. Here the choice of retracking threshold has

641 proven to be the critical factor to acquire high quality surface elevations and elevation changes.

642 The choice of 20% leading edge threshold level reduced the sensitivity to changes in the

643 scattering regime for low slope, high elevation areas. The functional-based retracking algorithm

644 used in the ESA LRM processor corresponds roughly to a 50% threshold level (Wingham et al.,

645 2006a), which appears to suffer from a higher sensitivity to changes in the scattering properties

646 (volume scattering) of the near-surface firn, as the range is reference higher up (later in time) on

647 the leading edge of the waveform. This effect can be seen in Figure 2a, and that the observed

648 negative elevation bias (Table-1) for ESA-LRM (-1.0 m) fit well with the bias for the 50% LRM

649 threshold value shown in Figure 2a. This makes the algorithm more sensitive to annual and sub-

650 annual changes in snow-packs volume/surface scattering ratio, which can produce spurious

651 changes in elevation due to changes in the near surface dielectric properties. This is clearly

652 shown in patterns of ESA product derived elevation changes (Figure 3) where a large elevation

653 bias was introduced by the 2012-melt event (Nilsson et al., 2015a). The 20% threshold is less

654 sensitive to these types of changes (Table 1 & 2) and the results are in agreement with previous

655 work that has demonstrated that the 20% threshold best represents the mean surface inside the

656 footprint when exposed to a combination of surface and volume scattering (Davis, 1997).

657   Surface elevation changes, derived from multi-temporal radar altimetry observations, are

658 typically corrected for their correlation to changes in the radar waveform shape. This is to

659 reduce the effect of changes in the volume/surface scattering ratio of the ice sheets surface

660 (Davis, 2005; Flament and Rémy, 2012; Wingham et al., 2006b; Zwally et al., 2005). This

661 inherently adds to the complexity of the processing and analysis, introducing new biases and

662 error sources in the estimated parameters. For the processing approach presented here many

663   of these steps can be omitted or reduced, as they are an inherent part of the improved

664   waveform retracking. There have been attempts to remove spurious step-changes in elevation

665   resulting from sudden changes in surface scattering characteristics (caused by the 2012 melt

666   event) apparent in the ESA Baseline-B L2 data through post-processing strategies (Nilsson et

667   al., 2015c and McMillan et al., 2016), but such approaches spread the bias over a longer period

668   of time making the "jumps" less noticeable in the time series by removing the step-change but

669   introduces longer-timescale bias of equal magnitude as the scattering layer is buried by less

670   reflective snow and low-density firn.

671   The result of the validation procedure shows a larger slope dependent bias in the ESA

672   data, both in the elevation and elevation changes (Figure-1). This is especially true for the

673   surface elevations, which can be seen in the figures of precision and accuracy (Figure 1a and

674   1c), where both figures show clear linear slope for the ESA surface heights. In comparison,

675   estimated elevations from JPL-product show relatively stable statistics over the entire slope

676   range above 0.2°. The validation of the estimated surface elevation changes, seen in (Figure

677   1b) and (Figure 1d), shows the effect of the 2012 melt event on the ESA derived elevation

678   changes below 0.2°. Further, the accuracy of the ESA derived changes show a clear negative

679   trend as function of increased surface slope. The derived precision of the surface elevation

680   change increases dramatically above 0.5°, as more complex topography is measured.

681   The JPL CryoSat-2 processing methodology produces seasonal amplitudes that are in

682   good agreement with those derived from ICESat data, further indicating the processors abilities

683   to track real and physical changes of the ice sheets surface. The current ESA implementation

684   produces noisier estimates of elevation change, as indicated by the larger standard deviations

685   of the residuals in the ESA solutions for the surface-fit and crossover-method. Figure 5 further

686   shows an amplitude bias in the ESA data compared to the corresponding ICESat reference

687   amplitudes. The bias is constant above the Greenland ELA located around 2000 m in altitude

688   but increases linearly as elevations decrease below this. The linear increase in amplitude

689   seems to be connected to the higher and more variable precipitation in the ablation zone where

690   changes in the variable snow cover produces changes in apparent surface height. This is less

691   prominent for the JPL SIN and LRM retrackers. The estimated seasonal phase in Figure 5c and

692   5d show that both JPL and ESA CryoSat-2 elevation products can adequately resolve the

693   seasonal maximum of the accumulation signal. Both products provide a timing of the maximum

694   to the month of July over the entire ice sheet, independent of elevation. Assessing the CryoSat-

695   2 derived maximum one does however notice a difference between CryoSat-2 and the

696   reference ICESat dataset. This constitutes roughly a ±1 month difference depending on the

697   elevation and the location. The cause of this difference can be attributed to the temporal

698   sampling of the ICESat mission. During the mission, due to degraded laser lifespan, data was

699   only collected in campaign mode during the spring and winter times corresponding to roughly

700   two months of measurements for each period. When the CryoSat-2 data was resampled to

701   coincide with the ICESat temporal sampling the same elevation and spatial pattern in the phase

702   of the maximum seasonal amplitude was observed as determined from the ICESat data. No

703   corresponding change in amplitude was observed. This was done by selecting CryoSat-2 data

704   corresponding to the same unique months available in the total ICESat record.

705   The two independent methods used to estimate the volume change of the Greenland Ice

706   Sheet produce consistent volume change estimates. This was especially true for volume

707   changes derived from the JPL elevations, with a discrepancy of less than 1 $km^3 a^{-1}$ between

708   methods. The two methods provided the same estimate of integrated volume change but the

709   use of the surface-fit is recommended as it produces higher spatial sampling compared to the

710   crossover-method and lower errors. The good agreement between the methods further

711   indicates a strong reliability in the estimated volume change rates of the Greenland Ice Sheet

712   over the four-year period. It also shows the ability of CryoSat-2 to capture both small and large-

713   scale spatial patterns in the rugged topography along the coastline and in the interior of

714   Greenland. This is especially true in the major outlet glacier systems (e.g., Zachariæ Isstrøm,

715   Nioghalvfjerdsfjorden and Storstrømmen).

716   Studying the northern parts of the Greenland Ice Sheet we find that CryoSat-2 captures

717   both intricate and complex behavior in the marginal areas of the ice sheet. This is exemplified in

718   the NE regions of Greenland (Figure 6) near Zacahariæ Isstrøm, Nioghalvfjerdsfjorden and

719   Storstrømmen, which all show complex and localized patterns of elevation change. Here,

720   Nioghalvfjerdsbrae shows very small changes in elevation during the observational time-span,

721   while Zacahariæ Isstrøm, its major neighbor shows large negative trends in elevation change.

722   The observed behavior agrees with the observations made in recent studies by Khan et al.

723   (2014) and Mouginot et al. (2015) who document rapid retreat and drawdown of the ice-front

724   position of the Zacahariæ Isstrøm beginning in 2012. Storstrømmen outlet glacier system also

725   appears to show signs of rapid thinning at low elevations near the ice-front position while a large

726   positive signal is observed roughly 100 km upstream of the terminus. This pattern has also been

727   observed by Joughin et al., (2010) and Thomas et al., (2009), using airborne altimetry and

728   surface velocity mapping. Rates of elevation change from ICESat and CryoSat-2 data show

729   good agreement in basin-scale trends (Figure 6b,c) over the 2003-2009 and 2010-2015 time

730   spans.

731   Mass loss of the Greenland Ice Sheet was estimated for comparison purposes from the Gravity

732   Recovery Climate Experiment (GRACE) satellite for the matching CryoSat-2 time period of

733   2011-2015 (Wiese et al., 2015; Watkins et al., 2015). Converting the estimated mass change to

734   volume change, assuming no changes in firn air content over the study period and an ice

735   density of 917 kg m^{-3} (assessment of changes in firn air content is out of the scope of this

736   paper), gives an ice sheet wide rate of -305 ± 38 km^3 a^{-1} (updated to Schlegel et al., 2016). This

737   estimate is corrected for volume changes from peripheral glaciers that lost volume at a rate of

738   approximately -40 ± 27 km^3 a^{-1} (Box, 2013; Fettweis et al., 2012; Noël et al., 2015). This

739   estimate of peripheral glacier change is in agreement with the estimated volume change of –41

740   ± 8 km^3 a^{-1} from Gardner et al, (2013). The volume rate derived from GRACE data agrees well

741   with our estimated rate from CryoSat-2, where both results are within the 1σ uncertainty of each

742   other and neglecting changes in firn air content over the period of study. The observed volume

743   change rates estimated from this study are within the range of previous studies, ranging from -

744   186 to -309 km^3 a^{-1} for the time period 2003-2009, summarized by Csatho et al. (2014), using

745   the same mass to volume conversion applied to the GRACE data. A more recent study by Helm

746   et al. (2014) of -375 ± 24 km^3 a^{-1} agrees within uncertainties when differences in observation

747   periods (2011 – 2014 vs. 2011 - 2015) are taken into accounted. From this comparison we find

748   that our estimate spans both the estimate of Csatho et al. (2014) and the mass loss estimated

749   from GRACE, while acknowledging the varied time spans of the different studies.

9 – Summary and Conclusion

751   We conclude that the use of an adaptive retracker for the SIN-mode, based on the maximum

752   gradient method, and the use of 20% threshold retracker for the LRM-mode provide improved

753   performance to the retracker currently used for the ESA L2 elevation products. It is further

754   important, especially for the SIN-mode, to apply a leading edge discriminator to identify and

755   track the leading edge of the waveform. The functional model currently employed in the ESA

756   processor has, to the author's knowledge, no such discriminator currently implemented. This is

757   important in the SIN-mode, as it often contains multiple surface returns. The single-return model

758   applied in the ESA processor will here have issues fitting a waveform containing multiple

759   surface returns resulting in retrack jitter (Helm et al., 2014).

760   Using the new CryoSat-2 processing methodology for the LRM and SIN-mode we

761   determine the volume change of the Greenland Ice Sheet to be -289 ± 20 km^3 a^{-1} during the

762   period January 2011 to January 2015. The validation against airborne ATM surface elevations

763   and elevation changes showed an average improvement in the RMSE of the measured

764 elevations of 68% and 27% for the LRM and SIN mode respectively compared to ESA Baseline-

765 B L2 products. The new methodology also provide improved elevation changes with an

766 reduction in RMSE of 55% and 40% for the LRM and SIN mode respectively, compared to their

767 ESA L2 derived counterparts.

768   The methodology also showed less sensitivity to changes in near-surface scattering

769 properties than equivalent ESA products. The new processing methodology showed little effect

770 of slope-induced errors, providing better performance in the marginal areas of the ice sheets.

771 These improvements to the CryoSat-2 processing mitigate the need for post-processing to

772 correct correlations between changes in surface elevation and changes in the waveform shape

773 (i.e. backscatter and leading edge width etc.) that can introduce biases and add to the

774 complexity of the processing and analysis.

775   The presented CryoSat-2 processing methodology provides a lower intrinsic error in the

776 measured elevation, elevation change and volume change estimates, all of which will facilitate

777 improved understanding of the geophysical process leading to changes in land ice elevation.

778 Given the release of the ESA Baseline-C, which provides improved corrections and processing

779 mainly for the L1B product, further improvements are expected in the near future.

780 The complete set of grids used in this study is available for the public from the main author (J.

781 Nilsson) upon request and are provided in geotiff format.

Acknowledgement

783 We are deeply thankful for the guidance of Laurence Gray and support of David Burgess. We

784 also thank Sebastian Bjerregaard Simonsen for very fruitful discussions. Further, we thank

785 Frank Paul at the University of Zurich for providing us with polygon-outlines of the Greenland Ice

786 Sheet and to the European Space Agency for providing their CryoSat-2 L1b product. We are

787 very grateful to the editor E. Berthier, the reviewer L. Schröder and an anonymous reviewer for

788   their thoughtful and thorough comments that greatly improve the writing and content of the

789   manuscript. We also thank Nicole-Jeanne Schlegel and David Wiese at the Jet Propulsion

790   Laboratory for the use of their GRACE analysis. This publication is contribution 86 of the Nordic

791   Centre of Excellence SVALI funded by the Nordic Top-level Research Initiative. This work was

792   supported by funding from the NASA Cryosphere program. The research was conducted at the

793   Jet Propulsion Laboratory, California Institute of Technology under contract with NASA.

794   References

795   Abulaitijiang, A., Andersen, O. B. and Stenseng, L.: Coastal sea level from inland CryoSat-2

796   interferometric SAR altimetry, Geophys. Res. Lett., 42(6), 1841–1847,

797   doi:10.1002/2015GL063131, 2015.

798   Arthern, R., Wingham, D. and Ridout, A.: Controls on ERS altimeter measurements over ice

799   sheets: Footprint-scale topography, backscatter fluctuations, and the dependence of microwave

800   penetration depth on satellite orientation, J. Geophys. Res. Atmos., 106(D24), 33471–33484,

801   doi:10.1029/2001JD000498, 2001.

802   Bales, R. C., Guo, Q., Shen, D., McConnell, J. R., Du, G., Burkhart, J. F., Spikes, V. B., Hanna,

803   E. and Cappelen, J.: Annual accumulation for Greenland updated using ice core data developed

804   during 2000-2006 and analysis of daily coastal meteorological data, J. Geophys. Res. Atmos.,

805   114(6), doi:10.1029/2008JD011208, 2009.

806   Bamber, J. L.: Ice sheet altimeter processing scheme, Int. J. Remote Sens., 15(4), 925–938,

807   doi:10.1080/01431169408954125, 1994.

808   Borsa, A. A., Moholdt, G., Fricker, H. A. and Brunt, K. M.: A range correction for ICESat and its

809   potential impact on ice-sheet mass balance studies, Cryosphere, 8(2), 345–357, doi:10.5194/tc-

810   8-345-2014, 2014.

811   Bouzinac, C.: CryoSat product handbook, European Space Agency, ESA,

812   (https://earth.esa.int/documents/10174/125272/CryoSat_Product_Handbook) (latest checked

813   October 2016), 2014.

814   Box, J. E.: Greenland Ice Sheet Mass Balance Reconstruction. Part II: Surface Mass Balance

815   (1840–2010)*, J. Clim., 26(18), 6974–6989, doi:10.1175/JCLI-D-12-00518.1, 2013.

816   Brenner, A. C., Blndschadler, R. A., Thomas, R. H. and Zwally, H. J.: Slope-induced errors in

817   radar altimetry over continental ice sheets, J. Geophys. Res., 88(C3), 1617,

818   doi:10.1029/JC088iC03p01617, 1983.

819   Brenner, A. C. ., DiMarzio, J. P. . and Zwally, H. J. .: Precision and accuracy of satellite radar

820   and laser altimeter data over the continental ice sheets, IEEE Trans. Geosci. Remote Sens.,

821   45(2), 321–331, doi:10.1109/TGRS.2006.887172, 2007.

822   Csatho, B. M., Schenk, A. F., van der Veen, C. J., Babonis, G., Duncan, K., Rezvanbehbahani,

823   S., van den Broeke, M. R., Simonsen, S. B., Nagarajan, S. and van Angelen, J. H.: Laser

824   altimetry reveals complex pattern of Greenland Ice Sheet dynamics., Proc. Natl. Acad. Sci. U. S.

825   A., 111(52), 18478–83, doi:10.1073/pnas.1411680112, 2014.

826   Davis, C. H.: Surface and volume scattering retracking algorithm for ice sheet satellite altimetry,

827   IEEE Trans. Geosci. Remote Sens., 31(4), 811–818, doi:10.1109/36.239903, 1993.

828   Davis, C. H.: A robust threshold retracking algorithm for measuring ice-sheet surface elevation

829   change from satellite radar altimeters, IEEE Trans. Geosci. Remote Sens., 35(4), 974–979,

830   doi:10.1109/36.602540, 1997.

831   Davis, C. H.: Snowfall-Driven Growth in East Antarctic Ice Sheet Mitigates Recent Sea-Level

832   Rise, Science (80-.)., 308(5730), 1898–1901, doi:10.1126/science.1110662, 2005.

833   Davis, C. H. and Ferguson, A. C.: Elevation change of the antarctic ice sheet, 1995-2000, from

834   ERS-2 satellite radar altimetry, IEEE Trans. Geosci. Remote Sens., 42(11), 2437–2445,

835   doi:10.1109/TGRS.2004.836789, 2004.

836   Ettema, J., Van Den Broeke, M. R., Van Meijgaard, E., Van De Berg, W. J., Bamber, J. L., Box,

837   J. E. and Bales, R. C.: Higher surface mass balance of the Greenland ice sheet revealed by

838   high-resolution climate modeling, Geophys. Res. Lett., 36(12), 1–5,

839   doi:10.1029/2009GL038110, 2009.

840   Fettweis, X., Franco, B., Tedesco, M., van Angelen, J. H., Lenaerts, J. T. M., van den Broeke,

841   M. R. and Gallée, H.: Estimating Greenland ice sheet surface mass balance contribution to

842   future sea level rise using the regional atmospheric climate model MAR, Cryosph., 7, 469–489,

843   doi:10.5194/tcd-6-3101-2012, 2012.

844   Flament, T. and Rémy, F.: Dynamic thinning of Antarctic glaciers from along-track repeat radar

845   altimetry, J. Glaciol., 58(211), 830–840, doi:10.3189/2012JoG11J118, 2012.

846   Galin, N., Wingham, D. J., Cullen, R., Fornari, M., Smith, W. H. F. and Abdalla, S.: Calibration of

847   the CryoSat-2 interferometer and measurement of across-track ocean slope, IEEE Trans.

848   Geosci. Remote Sens., 51(1), 57–72, doi:10.1109/TGRS.2012.2200298, 2013.

849   Gardner, A. S., Moholdt, G., Cogley, J. G., Wouters, B., Arendt, A. a, Wahr, J., Berthier, E.,

850   Hock, R., Pfeffer, W. T., Kaser, G., Ligtenberg, S. R. M., Bolch, T., Sharp, M. J., Hagen, J. O.,

851   van den Broeke, M. R. and Paul, F.: A reconciled estimate of glacier contributions to sea level

852   rise: 2003 to 2009., Science, 340(6134), 852–7, doi:10.1126/science.1234532, 2013.

853   Gray, L., Burgess, D., Copland, L., Cullen, R., Galin, N., Hawley, R. and Helm, V.:

854   Interferometric swath processing of Cryosat data for glacial ice topography, Cryosph., 7(6),

855   1857–1867, doi:10.5194/tc-7-1857-2013, 2013.

856   Gray, L., Burgess, D., Copland, L., Demuth, M. N., Dunse, T., Langley, K. and Schuler, T. V.:

857   CryoSat-2 delivers monthly and inter-annual surface elevation change for Arctic ice caps,

858   Cryosph., 9(5), 1895–1913, doi:10.5194/tc-9-1895-2015, 2015.

859   Helm, V., Humbert, A. and Miller, H.: Elevation and elevation change of Greenland and

860   Antarctica derived from CryoSat-2, Cryosph., 8(4), 1539–1559, doi:10.5194/tc-8-1539-2014,

861   2014.

862   Herzfeld, U. C.: Least-squares collocation, geophysical inverse theory and geostatistics: a bird's

863   eye view, Geophys. J. Int., 111(2), 237–249, doi:10.1111/j.1365-246X.1992.tb00573.x, 1992.

864   Howat, I. M., Smith, B. E., Joughin, I. and Scambos, T. A.: Rates of southeast Greenland ice

865   volume loss from combined ICESat and ASTER observations, Geophys. Res. Lett., 35(17), 1–5,

866   doi:10.1029/2008GL034496, 2008.

867   Howat, I. M., Negrete, A. and Smith, B. E.: The Greenland Ice Mapping Project (GIMP) land

868   classification and surface elevation data sets, Cryosph., 8(4), 1509–1518, doi:10.5194/tc-8-

869   1509-2014, 2014.

870   Joughin, I., Smith, B. E., Howat, I. M., Scambos, T. and Moon, T.: Greenland flow variability

871   from ice-sheet-wide velocity mapping, J. Glaciol., 56(197), 415–430,

872   doi:10.3189/002214310792447734, 2010.

873   Keith Raney, R.: The delay/doppler radar altimeter, IEEE Trans. Geosci. Remote Sens., 36(5),

874   1578–1588, doi:10.1109/36.718861, 1998.

875   Khan, S. a, Kjaer, K. H., Bevis, M., Bamber, J. L., Wahr, J., Kjeldsen, K. K., Bjork, A. a,

876   Korsgaard, N. J., Stearns, L. a, van den Broeke, M. R., Liu, L., Larsen, N. K. and Muresan, I. S.:

877   Sustained mass loss of the northeast Greenland ice sheet triggered by regional warming, Nat.

878   Clim. Chang., 4(4), 292–299, doi:10.1038/nclimate2161, 2014.

879   Khvorostovsky, K. S.: Merging and Analysis of Elevation Time Series Over Greenland Ice Sheet

880   From Satellite Radar Altimetry, IEEE Trans. Geosci. Remote Sens., 50(1), 23–36,

881   doi:10.1109/TGRS.2011.2160071, 2012.

882   Krabill, W. B., Abdalati, W., Frederick, E. B., Manizade, S. S., Martin, C. F., Sonntag, J. G.,

883   Swift, R. N., Thomas, R. H. and Yungel, J. G.: Airborne laser altimetry mapping of the

884   Greenland ice sheet : application to mass balance assessment, J. Geodyn., 34, 357–376,

885   doi:10.1016/s0264-3707(02)00048-0, 2002.

886   Lacroix, P., Dechambre, M., Legrésy, B., Blarel, F. and Rémy, F.: On the use of the dual-

887   frequency ENVISAT altimeter to determine snowpack properties of the Antarctic ice sheet,

888   Remote Sens. Environ., 112, 1712–1729, doi:10.1016/j.rse.2007.08.022, 2008.

889   Lewis, S. M. and Smith, L. C.: Hydrologic drainage of the Greenland Ice Sheet, Hydrol.

890   Process., 23(14), 2004–2011, doi:10.1002/hyp.7343, 2009.

891 McMillan, M., Leeson, A., Shepherd, A., Briggs, K., Armitage, T. W. K., Hogg, A., Kuipers

892 Munneke, P., van den Broeke, M., Noël, B., van de Berg, W. J., Ligtenberg, S., Horwath, M.,

893 Groh, A., Muir, A. and Gilbert, L.: A high-resolution record of Greenland mass balance,

894 Geophys. Res. Lett., 43(13), 7002–7010, doi:10.1002/2016GL069666, 2016.

895 Moholdt, G., Nuth, C., Hagen, J. O. and Kohler, J.: Recent elevation changes of Svalbard

896 glaciers derived from ICESat laser altimetry, Remote Sens. Environ., 114(11), 2756–2767,

897 doi:10.1016/j.rse.2010.06.008, 2010.

898 Mouginot, J., Rignot, E., Scheuchl, B., Fenty, I., Khazendar, A., Morlighem, M., Buzzi, A. and

899 Paden, J.: Fast retreat of Zachariae Isstrom, northeast Greenland, Science (80-.)., 350(6266),

900 1357–1361, doi:10.1126/science.aac7111, 2015.

901 Nilsson, J., Vallelonga, P., Simonsen, S. B., Sørensen, L. S., Forsberg, R., Dahl-Jensen, D.,

902 Hirabayashi, M., Goto-Azuma, K., Hvidberg, C. S., Kjaer, H. A. and Satow, K.: Greenland 2012

903 melt event effects on CryoSat-2 radar altimetry, Geophys. Res. Lett., 42(10), 3919–3926,

904 doi:10.1002/2015GL063296, 2015a.

905 Nilsson, J., Sandberg Sørensen, L., Barletta, V. R. and Forsberg, R.: Mass changes in Arctic ice

906 caps and glaciers: implications of regionalizing elevation changes, Cryosph., 9(1), 139–150,

907 doi:10.5194/tc-9-139-2015, 2015b.

908 Nilsson, J, Forsberg, R and Sandberg Sørensen, L.: Cryosphere Monitoring from Satellites and

909 Aircrafts, Ph.D. thesis, Technical University of Denmark, Kgs. Lyngby, 2015c.

910 Noël, B., van de Berg, W. J., van Meijgaard, E., Kuipers Munneke, P., van de Wal, R. S. W. and

911 van den Broeke, M. R.: Evaluation of the updated regional climate model RACMO2.3: summer

912 snowfall impact on the Greenland Ice Sheet, Cryosph., 9(5), 1831–1844, doi:10.5194/tc-9-1831-

913 2015, 2015.

914 Poinar, K., Joughin, I., Das, S. B., Behn, M. D., Lenaerts, J. T. M. and van den Broeke, M. R.:

915 Limits to future expansion of surface-melt-enhanced ice flow into the interior of western

916 Greenland, Geophys. Res. Lett., 42(6), 1800–1807, doi:10.1002/2015GL063192, 2015.

917 Remy, F., Mazzega, P., Houry, S., Brossier, C. and Minster, J. F.: Mapping of the topography of

918 continental ice by inversion of satellite-altimeter data, J. Glaciol., 35(119), 98–107,

919 doi:10.3189/002214389793701419, 1989.

920 Remy, F., Flament, T., Blarel, F. and Benveniste, J.: Radar altimetry measurements over

921 antarctic ice sheet: A focus on antenna polarization and change in backscatter problems, Adv.

922 Sp. Res., 50(8), 998–1006, doi:10.1016/j.asr.2012.04.003, 2012.

923 Sasgen, I., van den Broeke, M., Bamber, J. L., Rignot, E., Sørensen, L. S., Wouters, B.,

924 Martinec, Z., Velicogna, I. and Simonsen, S. B.: Timing and origin of recent regional ice-mass

925 loss in Greenland, Earth Planet. Sci. Lett., 333–334, 293–303, doi:10.1016/j.epsl.2012.03.033,

926 2012.

927 N.-J. Schlegel, D.N. Wiese, E.Y. Larour, M.M. Watkins, J.E. Box, X. Fettweis, and M.R.

928 van den Broeke, Application of GRACE to the assessment of model-based estimates of

929 monthly Greenland Ice Sheet mass balance (2003–2012), The Cryosphere, 10, 1965-

930 1989, doi:10.5194/tc-10-1965-2016.

931 Shepherd, A., Ivins, E. R., A, G., Barletta, V. R., Bentley, M. J., Bettadpur, S., Briggs, K. H.,

932 Bromwich, D. H., Forsberg, R., Galin, N., Horwath, M., Jacobs, S., Joughin, I., King, M. A.,

933 Lenaerts, J. T. M., Li, J., Ligtenberg, S. R. M., Luckman, A., Luthcke, S. B., McMillan, M.,

934 Meister, R., Milne, G., Mouginot, J., Muir, A., Nicolas, J. P., Paden, J., Payne, A. J., Pritchard,

935 H., Rignot, E., Rott, H., Sorensen, L. S., Scambos, T. A., Scheuchl, B., Schrama, E. J. O.,

936 Smith, B., Sundal, A. V., van Angelen, J. H., van de Berg, W. J., van den Broeke, M. R.,

937 Vaughan, D. G., Velicogna, I., Wahr, J., Whitehouse, P. L., Wingham, D. J., Yi, D., Young, D.

938 and Zwally, H. J.: A Reconciled Estimate of Ice-Sheet Mass Balance, Science (80-.).,

939 338(6111), 1183–1189, doi:10.1126/science.1228102, 2012.

940 Sørensen, L. S., Simonsen, S. B., Nielsen, K., Lucas-Picher, P., Spada, G., Adalgeirsdottir, G.,

941 Forsberg, R. and Hvidberg, C. S.: Mass balance of the Greenland ice sheet (2003-2008) from

942   ICESat data - The impact of interpolation, sampling and firn density, Cryosphere, 5(1), 173–186,

943   doi:10.5194/tc-5-173-2011, 2011.

944   Sørensen, L. S., Simonsen, S. B., Meister, R., Forsberg, R., Levinsen, J. F. and Flament, T.:

945   Envisat-derived elevation changes of the Greenland ice sheet, and a comparison with ICESat

946   results in the accumulation area, Remote Sens. Environ., 160, 56–62,

947   doi:10.1016/j.rse.2014.12.022, 2015.

948   Thomas, R., Frederick, E., Krabill, W., Manizade, S. and Martin, C.: Recent changes on

949   Greenland outlet glaciers, J. Glaciol., 55(189), 147–162, doi:10.3189/002214309788608958,

950   2009.

951   Watkins, M. M., Wiese, D. N., Yuan, D., Boening, C. and Landerer, F. W.: Improved methods for

952   observing Earth's time variable mass distribution with GRACE using spherical cap mascons, J.

953   Geophys. Res. Solid Earth, 120(4), 2648–2671, doi:10.1002/2014JB011547, 2015.

954   Wenlu Qi and Braun, A.: Accelerated elevation change of Greenland's Jakobshavn glacier

955   observed by ICESat and IceBridge, IEEE Geosci. Remote Sens. Lett., 10(5), 1133–1137,

956   doi:10.1109/LGRS.2012.2231954, 2013.

957   Wiese, D. N., Yuan, D.-N., Boening, C., Landerer, F. W., and Watkins, M. M.: JPL GRACE

958   Mascon Ocean, Ice, and Hydrology Equivalent Water Height RL05M.1 CRI Filtered, Ver. 2,

959   PO.DAAC, CA, USA, doi:10.5067/TEMSC-OLCR5, 2015.

960   Wingham, D. J., Rapley, C. G. and Griffiths, H.: New Techniques in Satellite Altimeter Tracking

961   Systems, in Proceedings of the IGARSS Symposium, Zurich, pp. 1339–1344, ESA SP-254,

962   Zurich., 1986.

963   Wingham, D. J., Francis, C. R., Baker, S., Bouzinac, C., Brockley, D., Cullen, R., de Chateau-

964   Thierry, P., Laxon, S. W., Mallow, U., Mavrocordatos, C., Phalippou, L., Ratier, G., Rey, L.,

965   Rostan, F., Viau, P. and Wallis, D. W.: CryoSat: A mission to determine the fluctuations in

966   Earth's land and marine ice fields, Adv. Sp. Res., 37(4), 841–871,

967   doi:10.1016/j.asr.2005.07.027, 2006a.

968   Wingham, D. J., Shepherd, a, Muir, a and Marshall, G. J.: Mass balance of the Antarctic ice

969   sheet., Philos. Trans. A. Math. Phys. Eng. Sci., 364(1844), 1627–35,

970   doi:10.1098/rsta.2006.1792, 2006b.

971   Wouters, B., Martin-Espanol, A., Helm, V., Flament, T., van Wessem, J. M., Ligtenberg, S. R.

972   M., van den Broeke, M. R. and Bamber, J. L.: Dynamic thinning of glaciers on the Southern

973   Antarctic Peninsula, Science (80-.)., 348(6237), 899–903, doi:10.1126/science.aaa5727, 2015.

974   Zwally, H. J., Bindschadler, R. a, Brenner, a C., Major, J. a and Marsh, J. G.: Growth of

975   greenland ice sheet: measurement., Science, 246(4937), 1587–1589,

976   doi:10.1126/science.246.4937.1587, 1989.

977   Zwally, H. J., Giovinetto, M. B., Li, J., Cornejo, H. G. and Beckley, M. a: Mass changes of the

978   Greenland and Antarctica ice sheets and shelves and contributions to sea level rise: 1992-2002,

979   J. Glaciol., 51(175), 509, doi:10.3189/172756505781829007, 2005.

980   Zwally, H. J., Jun, L., Brenner, A. C., Beckley, M., Cornejo, H. G., Dimarzio, J., Giovinetto, M.

981   B., Neumann, T. a, Robbins, J., Saba, J. L., Donghui, Y. and Wang, W.: Greenland ice sheet

982   mass balance: distribution of increased mass loss with climate warming; 2003–07 versus 1992–

983   2002, J. Glaciol., 57(201), 88–102, doi:10.3189/002214311795306682, 2011.

984   Zwally, H. Jay, Mario B. Giovinetto, Matthew A. Beckley, and Jack L. Saba: Antarctic and

985   Greenland drainage systems, GSFC Cryospheric Sciences Laboratory, at

986   http://icesat4.gsfc.nasa.gov/cryo_data/ant_grn_drainage_systems.php, 2012

987   Tables:

988   *Table 1: Accuracy (Mean), precision (SD) and the total RMS-error (RMSE) of surface elevation*

989   *from CryoSat-2 observations compared to IceBridge ATM elevations. Here, the LRM mode*

990   *represents the interior of the ice sheet and SIN the marginal high relief areas.*

JPL	Mean (m)	SD (m)	RMSE (m)
LRM	0.00	0.43	0.45
SIN	-0.52	0.58	0.82
ESA	**Mean (m)**	**SD (m)**	**RMSE (m)**
LRM	-1.06	0.89	1.40
SIN	-0.90	1.05	1.13

991

992 *Table 2: Accuracy (Mean), precision (SD) and the total RMS-error (RMSE) of surface elevation*

993 *changes from CryoSat-2 derived from two independent methods [Surface Fit (SF) and the*

994 *Crossover (XO) method], compared to IceBridge ATM data.*

JPL - LRM	Mean (m)	SD (m)	RMSE (m)
SF	0.11	0.67	0.70
XO	0.24	0.72	0.78
ESA - LRM	Mean (m)	SD (m)	RMSE (m)
SF	0.25	1.51	1.57
XO	0.60	1.02	1.20
JPL - SIN	Mean (m)	SD (m)	RMSE (m)
SF	0.30	0.58	0.66
XO	-0.60	1.26	1.26
ESA - SIN	Mean (m)	SD (m)	RMSE (m)
SF	0.34	1.06	1.11
XO	-0.21	1.44	1.44

995
996

997   Table 3: Validation of four different DEMs, compared to IceBridge ATM elevation data. Based

998   on the weighted (number of samples) average of the four different ATM campaigns from 2011 to

999   2014. Elevation values at each ATM location were estimated by bilinear interpolation for each

1000   DEM product.

DEM	Mean (m)	SD (m)	RMSE (m)
AWI	-1.35	5.95	6.12
GIMP	-1.13	7.22	7.32
JPL	-0.87	6.31	6.39
ESA	-2.83	6.13	6.76

1001
1002

1003   *Table 4: Individual basin volume changes (km³a⁻¹) for the Surface-Fit (SF) and Crossover (XO)*

1004   *method for the JPL and ESA product for the time period Jan-2011 to Jan-2015, with*

1005   *corresponding volumetric error.*

Basin	SF – JPL	XO – JPL	SF - ESA	XO - ESA
1	-26 ± 8	-23 ± 12	-9 ± 14	-11 ± 15
2	5 ± 8	0 ± 13	31 ± 16	30 ±16
3	-38 ± 9	-34 ± 19	-46 ± 16	-31 ± 23
4	-36 ± 7	-37 ± 15	-42 ± 12	-16 ± 18
5	-19 ± 4	-27 ± 11	-19 ± 7	-6 ± 13
6	-72 ± 7	-71 ± 12	-75 ± 13	-79 ± 18
7	-56 ± 7	-51 ± 10	-41 ± 14	-35 ± 15
8	-48 ± 8	-45 ± 12	-23 ± 15	-27 ± 17
TOT	**-289 ± 20**	**-288 ± 37**	**-224± 38**	**-174 ± 48**

1006

1007   Figures:

1008

1009   *Figure 1: Validation of surface elevations (2012) (a,c) and surface elevation changes (2011-*

1010   *2014) (b,d) compared to IceBridge ATM, as a function of surface slope. The accuracy of the*

1011   *measurement is defined as the mean-value (Mean) of the CryoSat-2-ATM residuals and the*

1012   *precision as the standard deviation (SD).*
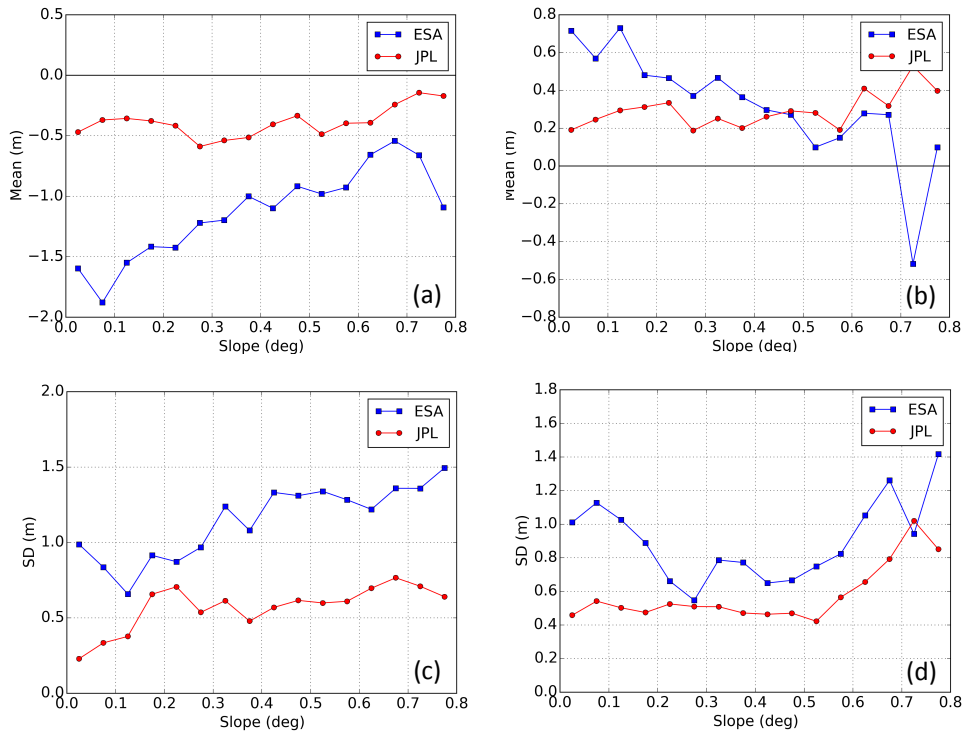
1013

1014

1015

1016

1017

1018
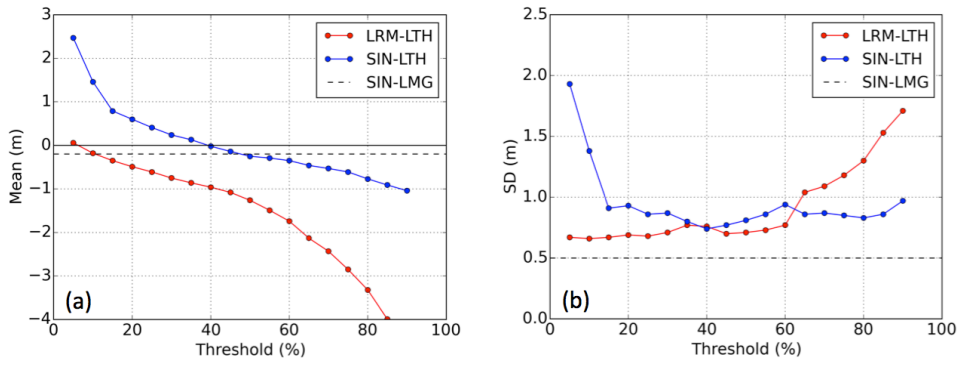
1019

1020   *Figure 2: Comparison of accuracy (a) and precision (b) as a function of the retracking threshold*

1021   *for the leading edge threshold retracker (LTH, dots) applied to the of the LRM (red) and SIN*

1022   *(blue) data and the leading edge maximum gradient retracker (LMG, dashed grey line) applied*

1023   *to the SIN data over Jakobshavn Isbræ and the region around the NEEM camp (77°27'N*

1024   *51°3.6'W). The accuracy (mean) and the precision (standard deviation) has for each threshold*

1025   *level been determined using near coincident ATM elevation, within a search radius of 50 m. The*

1026   *statistics was estimated using CryoSat-2 data from March-May 2013 and compared to ATM*

1027   *data from April 2013.*

1028

1029

1030

1031

1032
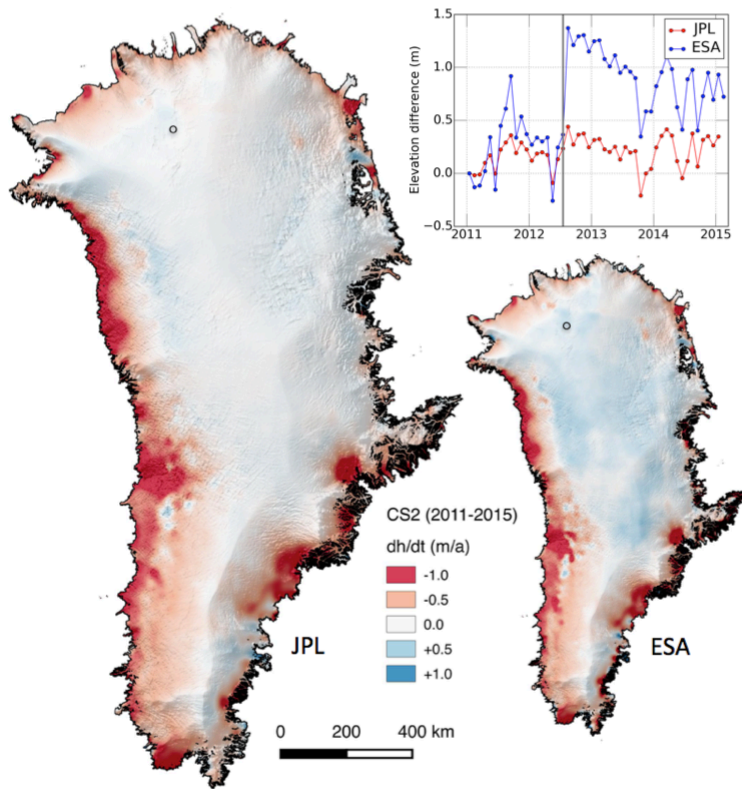
1033

1034 *Figure 3: 2011-2015 elevation changes estimated from the surface-fit methods for the estimated*

1035 *L2 products. The time series depicted in the figure has been extracted at the NEEM camp*

1036 *(77°27'N 51°3.6'W), indicated by the black circle in both maps. The time series show the effect*

1037 *of the 2012 melt event, indicated by the grey vertical line, on the retrieved surface elevations.*

1038 *The JPL product produced a total volume change of -289 ± 20 $km^3 a^{-1}$ while the estimated total*

1039 *volume change of the ESA product was -224 ± 38 $km^3 a^{-1}$. This corresponds to -29 versus 38*

1040 *$km^3 a^{-1}$ (H > 2000 m) and -259 versus -262 $km^3 a^{-1}$ (H < 2000 m) for the JPL and ESA product*

1041 *respectively. Images have been smoothed with a 10 km median filter for visualization purposes.*

1042 *The 1x1 km ice sheets mask used in this figure was constructed from polygons obtained from*

1043 *Frank Paul at the University of Zurich (personal communication).*
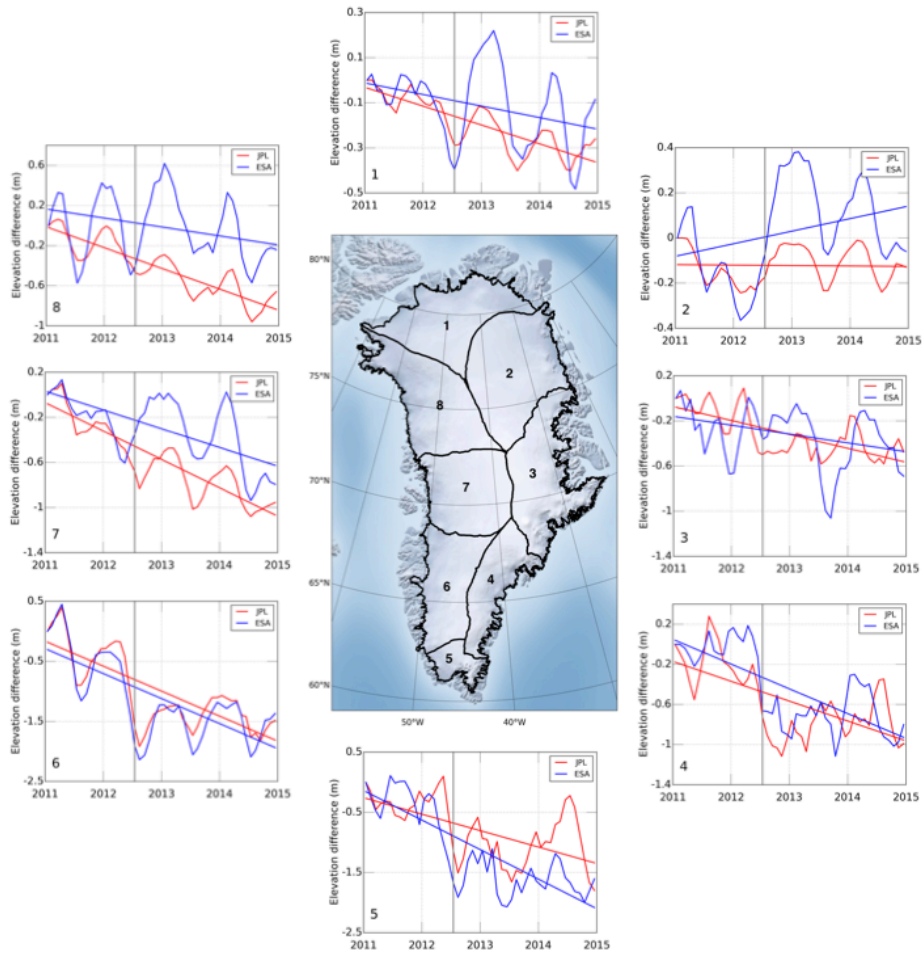
Figure 4. Monthly elevation change time-series for 8 large drainage basins of the Greenland Ice Sheet generated from the ESA (red) and the JPL solution (blue). Time-series have been smoothed using a 3-month moving average for improved visualization. The grey vertical line indicates the timing of the 2012 melt event.
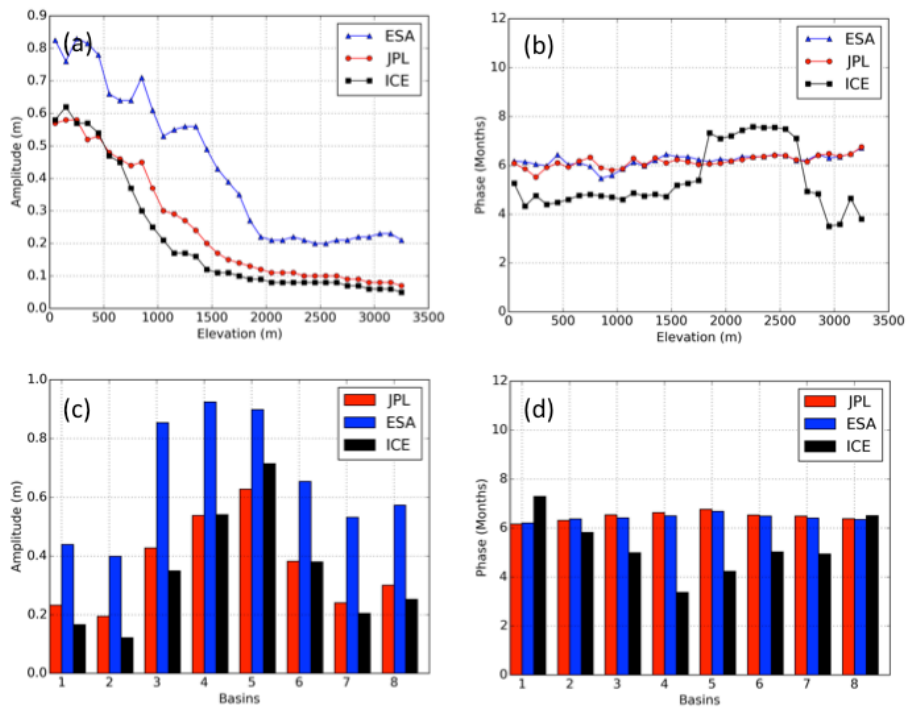
Figure 5: Estimated seasonal amplitude (a,c) and phase of the maximum amplitude (b,d) from the surface-fit method for CryoSat-2 [ESA (blue) and JPL (red)] compared to ICESat (ICE, black)). Values are compared using a search radius of 50 m, using the closest point within this distance, and the phase offset is referenced from 1st of January. The values of amplitude and phase are then binned according to elevation using the median value within 100 m intervals

Johan Nilsson 10/19/2016 10:15 AM
Deleted:
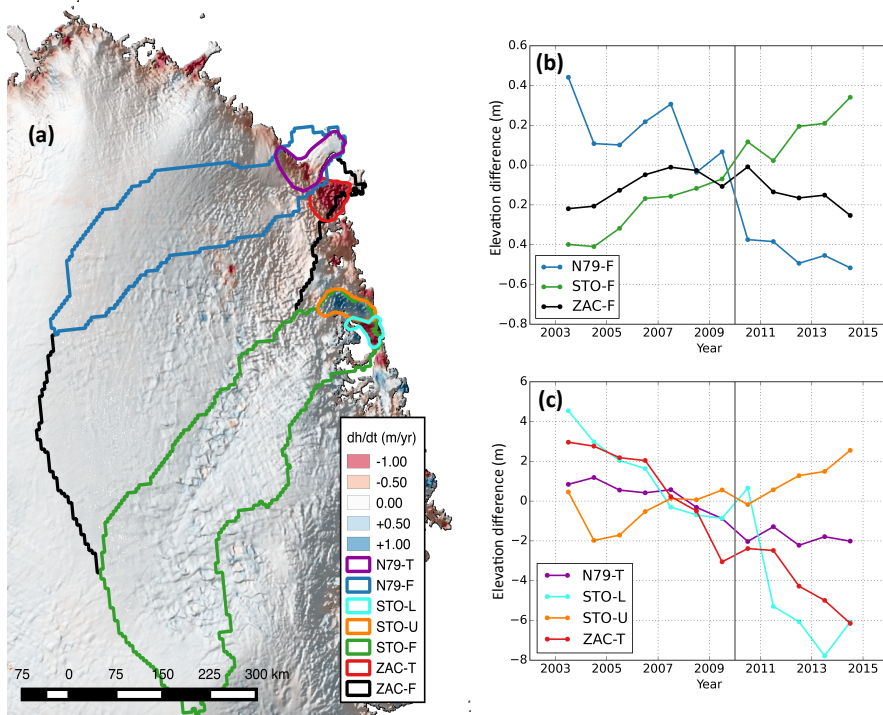
1064

1065 *Figure 6: Northeast part of the Greenland Ice Sheet showing surface elevation change (a) from*

1066 *CryoSat-2 JPL-solution (2011-2015), with corresponding hydrological basin outlines. The*

1067 *hydrological basins are separated into full basins size (b) and to the terminus areas (c). Sub-*

1068 *figures (b) and (c) shows a merged 12 year annual elevation time series from ICESat and*

1069 *CryoSat-2 for each color-coded area in (a). The derived elevation time series was formed using*

1070 *the surface-fit method described in Section (3.1) onto a 500 m grid to facilitate merging of the*

1071 *two data sets due to their difference in orbit characteristics. The elevation change map is*

1072 *overlaid onto the CryoSat-2 hill shaded DEM based on surface heights from Jul-2010 to Feb-*

1073 *2015. The annual 12-year time series was created from the surface-fit method by binning the*

1074 *monthly values into annual values using the median of the corresponding 12 months.*

1075

Rebuttal to editor for tc-2016-109

We would like to thank the editor for accepting our manuscript for publication and yet again for his valuable comments. As requested we have corrected the following last comments form the editor in the manuscript and provided tracked changes.

The editor's comments are marked using (E) and the corresponding response below with (R).

Main manuscript:

(E) L810. Schlegel et al., 2016 should appear in the reference list.

(R) Changed accordingly

(E) L891. "We very grateful to the editor". "are" missing

(R) Changed accordingly

(E) L1121. "as a function retracking threshold". "of the" missing

(R) Changed accordingly

(E) L1158. mention in the legend of this figure that the time series compare the result of two retrackers (as you explain well in the legend of Figure 5 for example).

(R) Extended the first sentence to describe the two solutions shown in the figure